

# Neutron Skins: Weak Elastic Scattering and Neutron Stars

Juliette M. Mammei<sup>1</sup>, Charles J. Horowitz<sup>2</sup>, Jorge Piekarewicz<sup>3</sup>,  
Brendan Reed<sup>4</sup>, and Concettina Sfienti<sup>5</sup>

<sup>1</sup>Department of Physics and Astronomy, University of Manitoba,  
Winnipeg, MB, Canada, R3T4E7; email:  
jmammei@physics.umanitoba.ca

<sup>2</sup>Department of Physics, Indiana University, Bloomington, IN  
47405, USA; email: horowit@indiana.edu

<sup>3</sup>Department of Physics, Florida State University Tallahassee, FL  
32306-4350

<sup>4</sup>Theoretical Division, Los Alamos National Laboratory, Los  
Alamos, New Mexico 87545, USA

<sup>5</sup>Institut für Kernphysik, Johannes Gutenberg-Universität Mainz,  
Germany, D-55099

November 13, 2023

## Abstract

The recently completed PREX-2 campaign—which measured the weak form factor of lead at an optimal momentum transfer—has confirmed that the neutron skin of lead is relatively large and has provided a precise determination of the interior baryon density of a heavy nucleus. In turn, the measured form factor can be related to various nuclear and neutron-star properties. Astrophysical observations by the NICER mission have benefited from improvements in flux, energy resolution, and notably, timing resolution. NICER has the capability to measure pulse profile data, which enables simultaneous mass-radius determinations. During the next decade, measurements in astrophysics, gravitational-wave astronomy, and nuclear physics are expected to provide a wealth of more precise data. In this review we provide an overview of the current state of neutron skin measurements and offer insights into the prospects for the future.

## 1 INTRODUCTION

We are living in a very exciting time for nuclear physics and astrophysics. The ability to measure properties of individual nucleons and complex nuclei with

ever higher precision will inform nuclear theory in areas of relevance to the extreme environments found within neutron stars. In particular, parity-violating electron scattering (PVES) is a powerful, yet challenging, experimental method that has been employed in experiments like PREX-2 and CREX. By relying exclusively on the electroweak interaction, PVES uncovers the inner workings of atomic nuclei in a model independent way. Unlike hadronic experiments that suffer from large and uncontrolled systematic errors, PVES offers sharp and critical insights into fundamental aspects of the nuclear dynamics. Furthermore, the scientific community is benefiting greatly from the emergence of neutrino, electromagnetic and gravitational-wave observatories worldwide, spearheading the new era of multi-messenger astronomy. The deployment of advanced telescopes such as the Neutron-star Interior Composition Explorer (NICER), the Chandra X-ray Observatory, and the XMM-Newton mission among others, is revolutionizing our ability to observe and analyze neutron stars. In turn, the historic detection of gravitational waves from binary neutron-star mergers is providing fundamental new insights into the astrophysical site for the creation of the heavy elements and on the nature of dense matter. Together with future PVES experiments, these telescopes will provide fundamental information on the nuclear equation of state (EOS), which quantifies how the pressure support against gravitational collapse evolves as a function of density. In this article, we will describe the profound connection between neutron stars and nuclei. We will discuss neutron rich matter and the observables that are particularly sensitive to the equation of state. We will describe the PREX-2 and CREX campaigns and the extraction of model independent weak form factors. Finally, we will survey some future measurements—both earth- and space-based—which will further our understanding of the nuclear theory needed to understand the structure, dynamics, and composition of neutron stars.

## 2 Neutron stars and neutron rich matter EOS

Neutron stars are compact objects more massive than the Sun but only about 12 km in radius [1, 2]. The first neutron star (NS) was discovered as a radio pulsar in 1967 by Jocelyn Bell-Burnell [3]. The densest known objects this side of black holes, their central density is at least a few times larger than the density found in the interior of atomic nuclei, providing exciting laboratories to study quantum chromodynamics (QCD) as well as gravitational and electromagnetic fields under extreme conditions. In this section we summarize the most salient features of neutron rich matter.

### 2.1 Neutron star structure

The structure of a neutron star is described theoretically by the Tolman-Oppenheimer-Volkoff (TOV) equations [5], which represent the generalization of Newtonian gravity to the domain of general relativity. The structure of a neutron star is not completely understood—even the maximum mass of a star is not known—

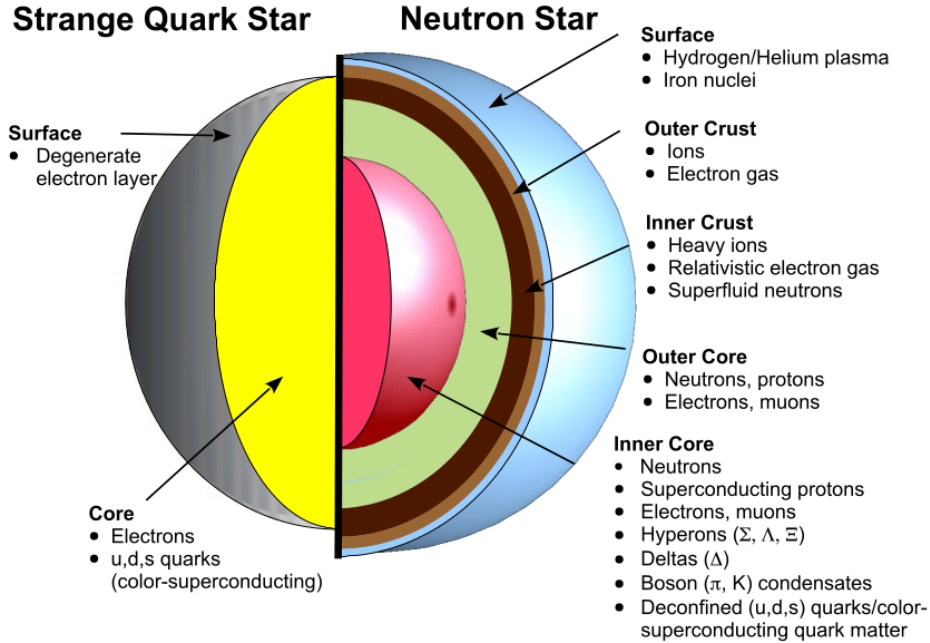


Figure 1: The assumed structure of a neutron star[4], consisting of a surface, an outer and inner crust, and an outer and inner core. These regions are defined by dramatic changes in structure and composition. The traditional view of a neutron star is compared against a possible model of a strange quark star, which because of a presumed phase transition, often result in a smaller radius for a given mass.

but the general description (see Fig. 1) is that there is an atmosphere and an envelope—which encompass the stellar surface—an outer and inner crust, and an outer and inner core. The crust is composed of a crystal lattice of neutron rich nuclei and relativistic electrons, while the outer core is a quantum liquid of neutron rich matter. The TOV equations describe the hydrostatic equilibrium where the force of gravity is balanced by the pressure of neutron rich matter. The mass and radius of a neutron star depend on the interactions in the dense matter of the star.

The composition of the inner core, in particular, is a mystery. Besides neutrons, protons, electrons, and muons, the inner core may contain exotic degrees of freedom such as hyperons (baryons containing strange quarks), meson (or boson) condensates, and deconfined quark matter. The emergence of new degrees of freedom is accompanied by a softening of the EOS, which often results in both smaller radii and a smaller maximum mass. In the case of models that predict the emergence of hyperons, this problem is commonly referred to in

the literature as the “hyperon puzzle” [6, 7, 8], since the predicted maximum neutron-star mass of some hyperon models is inconsistent with the observation of  $2M_{\odot}$  neutron stars [9, 10, 11, 12].

Also possible is the existence of strange quark stars, or at least stars with high-density cores made of equal numbers of massless up, down, and strange quarks. In this limit, the ground state is a color superconductor with a unique pairing scheme that couples color and flavor [13]. Unfortunately, it is now believed that the extreme densities required for such a phase to emerge can not be reached in the stellar cores. So assessing the impact of QCD at the densities of relevance to neutron stars remains an important challenge.

## 2.2 Neutron rich matter equation of state

The equation of state (EOS) of neutron rich matter is a relationship giving the pressure  $P = P(\epsilon)$  as a function of the energy density  $\epsilon$ . For two decades the neutron skin thickness of  $^{208}\text{Pb}$  has been identified as an ideal laboratory observable to constrain the EOS of neutron rich matter, see Fig. 2, particularly the poorly determined density dependence of the symmetry energy [14, 15, 16, 17]. The EOS of infinite nuclear matter at zero temperature is enshrined in the energy per particle which depends on both the conserved neutron ( $\rho_n$ ) and proton ( $\rho_p$ ) densities; here we assume that the electroweak sector has been “turned off”. Moreover, it is customary to separate the EOS into two contributions, one that represents the energy of symmetric ( $\rho_n = \rho_p$ ) nuclear matter and another one that accounts for the breaking of the symmetry (see Fig. 3). That is,

$$\frac{E}{A}(\rho, \alpha) - M \equiv \mathcal{E}(\rho, \alpha) = \mathcal{E}_{\text{SNM}}(\rho) + \alpha^2 \mathcal{S}(\rho) + \mathcal{O}(\alpha^4), \quad (1)$$

where  $\rho = (\rho_n + \rho_p)$  is the total baryon density given by the sum of neutron and proton densities, and  $\alpha = (\rho_n - \rho_p)/\rho$  is the neutron-proton asymmetry. The first-order correction to the energy of symmetric nuclear matter  $\mathcal{E}_{\text{SNM}}(\rho)$  is encoded in the symmetry energy  $\mathcal{S}(\rho)$ . The symmetry energy quantifies the increase in the energy per particle of infinite nuclear matter for systems with an isospin imbalance (e.g., more neutrons than protons). Furthermore, given the preeminent role of nuclear saturation, the energy of symmetric nuclear matter and the symmetry energy may be described in terms of a few bulk parameters that characterize their behavior around saturation density. In this review we focus on the density dependence of the symmetry energy [18]:

$$\mathcal{S}(\rho) = J + L \frac{(\rho - \rho_0)}{3\rho_0} + \dots \quad (2)$$

The first term ( $J$ ) represents the correction to the binding energy of symmetric nuclear matter, whereas the second term ( $L$ ) dictates how rapidly the symmetry energy increases with density. It is the slope of the symmetry energy  $L$  that displays a strong correlation to the neutron skin thickness of  $^{208}\text{Pb}$ . Given that symmetric nuclear matter saturates, namely, its pressure vanishes at saturation,

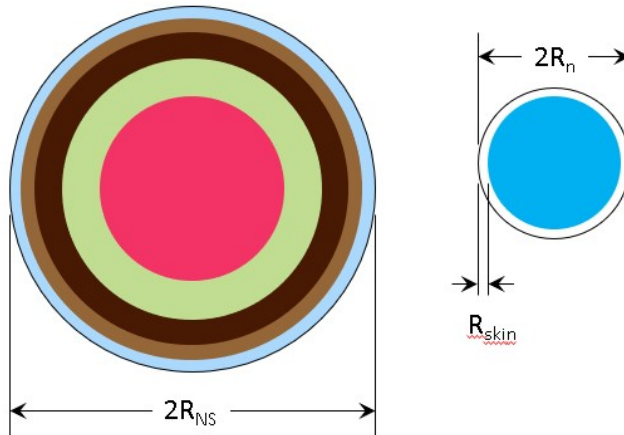


Figure 2: A neutron star (left) is 18 orders of magnitude larger than a Pb nucleus (right, not to scale). Nevertheless, the star is made of the same neutrons with the same strong interactions and equation of state. The structure of both objects depends on the pressure of neutron rich matter  $P$ . This pressure pushes neutrons out against surface tension and increases the neutron radius  $R_n$  of  $^{208}\text{Pb}$ . The radius of a neutron star  $R_{NS}$  also depends on  $P$ . Therefore a measurement of  $R_n$  in the laboratory has important implications for the structure of neutron stars.

the slope of the symmetry energy  $L$  is closely related to the pressure of pure neutron matter at saturation density. That is,

$$P_{\text{PNM}}(\rho_0) \approx \frac{1}{3}L\rho_0. \quad (3)$$

### 2.3 X-ray measurements of NS radii

Observations of NS masses and radii can help determine the EOS. Many NS have surface temperatures near  $10^6$  K and emit X-rays. Recently the NICER X-ray telescope has inferred masses and radii of some X-ray pulsars [19, 20, 21]. These measurements depend on pulse profile modeling of the light curve as a neutron star with hot spots rotates. When a hot spot is on the far side of the star some fraction of the radiation is still visible because of the gravitational curvature of space. Thus the depth of the light curve minimum provides a measure of the curvature and this depends on the star's mass and radius. We discuss this further in Sec. 6.2.

### 2.4 Gravitational wave measurements of NS deformability

The historic detection of gravitational waves emitted from the binary neutron star merger GW170817 has opened a brand new window into the Universe [22].

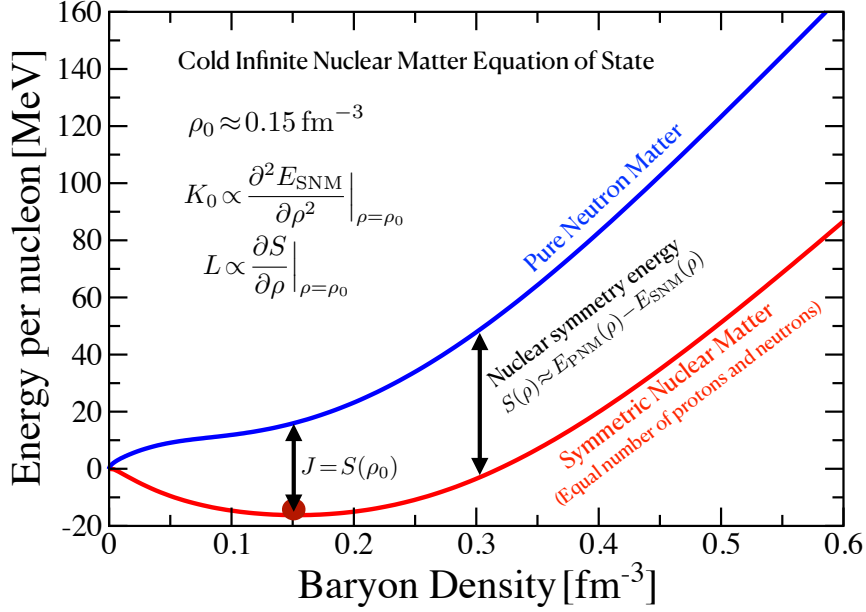


Figure 3: A depiction of the nuclear equation of state. The minimum in the energy per particle of symmetric nuclear matter (red) occurs at the saturation density of  $\rho_0 \approx 0.15 \text{ fm}^{-3}$ . The nuclear symmetry energy  $S(\rho)$  is approximated as the difference between the energy of pure neutron matter (blue) and symmetric nuclear matter. At saturation density this value is commonly referred to as  $J$ . The slope of the symmetry energy  $L$  is highly correlated to the neutron skin of neutron-rich nuclei as well as to the radii of neutron stars. The nuclear incompressibility  $K_0$  of symmetric nuclear matter is related to the curvature at saturation density and correlates strongly to the centroid energy of giant monopole resonances.

In particular, GW170817 is providing new insights into the astrophysical site for the rapid-neutron capture process - believed to be the mechanism behind the production of about half of the heavy elements beyond iron [23, 24, 25, 26] -and on the structure, dynamics, and composition of neutron stars [27, 28, 29, 30, 31, 32, 33, 34, 35, 36, 37, 38, 39, 40, 41, 42, 43, 44, 45, 46]

Binary neutron star mergers provide a few critical observables that inform the EOS of neutron rich matter. First, the chirp mass, defined as a linear combination of the individual masses of the two stars,

$$\mathcal{M} = \frac{(M_1 M_2)^{3/5}}{(M_1 + M_2)^{1/5}}, \quad (4)$$

is the most precise observable extracted from the gravitation wave profile [22]. Second, the tidal deformability encodes how a neutron star deforms in response

to the tidal field generated by its companion star [47, 48]. In the linear regime, the constant of proportionality connecting the external tidal forces to the star’s mass quadrupole is the dimensionless tidal deformability  $\Lambda$  defined as

$$\Lambda = \frac{2}{3}k_2 \left( \frac{c^2 R}{GM} \right)^5 \quad (5)$$

where  $k_2$  is the second Love number [49, 50, 51]. Although  $k_2$  is sensitive to the underlying EOS, most of the sensitivity is contained in the compactness parameter  $(c^2 R)/(GM)$  [52, 53, 54, 55, 56, 57, 28, 58]. An estimate by the LIGO-Virgo collaboration of the tidal deformability of a  $1.4 M_{\text{sun}}$  neutron star yields the relatively small value of  $\Lambda_{1.4} \lesssim 580$ , suggesting that neutron stars are dense objects with a small radius that are difficult to deform [30]. This implies a fairly soft EOS at intermediate densities. To our knowledge, GW170817 provides one of the very few indications that the EOS is soft.

### 3 Nuclear physics observables related to neutron rich matter

Given the importance of neutron skins in constraining the equation of state, in this section we describe our knowledge of nuclear sizes from both parity-conserving and parity-violating elastic electron scattering—highlighting two recent experimental efforts. While the main focus of this review is parity-violating electron scattering, we highlight its connection to coherent elastic neutrino nucleus scattering which also offers a promising model independent method for determining neutron densities.

#### 3.1 Nuclear sizes and elastic electron-nucleus scattering

The distribution of electric charge is a fundamental nuclear property that has been mapped with great accuracy along the valley of stability. Elastic electron scattering experiments pioneered by Hofstadter in the late 1950’s [59] and that continue to improve to this day [60, 61, 62, 63, 64], have painted the most compelling picture of the spatial charge distribution. Given that the electric charge of the nucleus is carried by the protons, elastic electron scattering provides a powerful tool for the determination of the ground-state proton density.

To appreciate the power of electron scattering in the determination of the charge distribution of atomic nuclei, we provide an expression for the cross section in the laboratory frame for when the electron scatters elastically from a spinless target. That is [65],

$$\left( \frac{d\sigma}{d\Omega} \right) = \left[ \frac{\alpha^2 \cos^2(\theta/2)}{4E^2 \sin^4(\theta/2)} \left( \frac{E'}{E} \right) \right] Z^2 F_{\text{ch}}^2(Q^2), \quad (6)$$

where  $Z$  is the electric charge of the nucleus,  $\alpha$  is the fine-structure constant,  $\theta$  is the scattering angle, and  $E$  and  $E'$  are the energies of the incoming and

scattered electrons, respectively. The expression in brackets is the Mott cross section which represents the scattering of a relativistic electron from a spinless and structureless target.

Deviations from the structureless limit are encoded in the charge form factor of the nucleus  $F_{\text{ch}}(Q^2)$  which depends on the exchanged photon four-momentum square  $Q^2 \equiv \mathbf{q}^2 - \omega^2 \approx \mathbf{q}^2$ .

Given that the form factor may be viewed as the Fourier transform of the spatial distribution, elastic electron scattering paints the most accurate picture of the distribution of charge in atomic nuclei [66].

To further illustrate the power of elastic electron-nucleus scattering in accurately determining nuclear sizes, we offer insights derived from the “symmetrized Fermi function”, which is defined as follows [67, 68]:

$$\rho_{\text{SF}}(r) = \rho_0 \frac{\sinh(c/a)}{\cosh(r/a) + \cosh(c/a)}, \text{ where } \rho_0 = \frac{3Z}{4\pi c(c^2 + \pi^2 a^2)}. \quad (7)$$

where  $c$  is the half-density radius and  $a$  the surface diffuseness. Although practically identical to the well-known two-parameter Fermi function, the symmetrized version displays better analytical properties that enables its Fourier transform—namely, the associated form factor—to be evaluated in closed form [67]. That is,

$$F_{\text{SF}}(q) = \frac{3}{qc((qc)^2 + (\pi qa)^2)} \left( \frac{\pi qa}{\sinh(\pi qa)} \right) \left[ \frac{\pi qa}{\tanh(\pi qa)} \sin(qc) - qc \cos(qc) \right], \quad (8)$$

Particularly insightful is the behavior of the symmetrized Fermi form factor in the limit of large momentum transfers, namely [68]:

$$F_{\text{SF}}(q) \rightarrow -6 \frac{\pi a}{\sqrt{c^2 + \pi^2 a^2}} \frac{\cos(qc + \delta)}{qc} e^{-\pi a q}; \quad \tan \delta \equiv \frac{\pi a}{c}. \quad (9)$$

This expression encapsulates many of the insights developed in the context of the conventional Fermi function, namely, diffractive oscillations controlled by the half-density radius  $c$  and an exponential falloff driven by the diffuseness parameter  $a$ , or rather  $\pi a$  [69, 70]. Yet, unlike the conventional Fermi function, the results presented here for the symmetrized version are exact. As such, all moments of the spatial distribution may also be evaluated exactly. For example, the mean square radius is given by

$$R^2 \equiv \langle r^2 \rangle = \frac{3}{5}c^2 + \frac{7}{5}(\pi a)^2. \quad (10)$$

### 3.2 Parity violating elastic electron-nucleus scattering

Given that photons are insensitive to the neutron distribution, many experimental facilities have been commissioned with the primary goal of mapping the neutron distribution of atomic nuclei. Most of these experimental facilities rely



on hadronic probes to map the neutron distribution. Although high statistics is the hallmark of hadronic experiments, the cost for such high efficiency are large systematic uncertainties associated with model dependencies and uncontrolled theoretical approximations. For a recent review on the large suite of experimental techniques devoted to map the neutron distribution and their associated uncertainties see [71].

To eliminate the dependence on hadronic probes, Donnelly, Dubach, and Sick realized more than three decades ago that parity-violating electron scattering (PVES) offers a uniquely clean probe of neutron densities that is free from strong-interaction uncertainties [72]. The pioneering Lead Radius EXperiment (PREX) at the Jefferson Laboratory (JLab) has fulfilled this vision by providing the first model-independent determination of the weak-charge form factor of  $^{208}\text{Pb}$ , albeit at a single value of the momentum transfer [73, 74].

Defined as the fractional difference between the elastic cross section for right-handed relative to left-handed polarized electrons, the parity violating asymmetry is defined as follows:

$$A_{PV}(Q^2) = \frac{\left(\frac{d\sigma}{d\Omega}\right)_R - \left(\frac{d\sigma}{d\Omega}\right)_L}{\left(\frac{d\sigma}{d\Omega}\right)_R + \left(\frac{d\sigma}{d\Omega}\right)_L} = \frac{G_F Q^2}{4\pi\alpha\sqrt{2}} \frac{Q_{\text{wk}} F_{\text{wk}}(Q^2)}{Z F_{ch}(Q^2)}, \quad (11)$$

where  $G_F$  is the Fermi constant,  $Q_{\text{wk}} = NQ_{\text{wk}}^n + ZQ_{\text{wk}}^p$  is the weak charge of the nucleus, and  $F_{\text{wk}}(Q^2)$  is the associated weak charge form factor, with  $F_{\text{wk}}(Q^2=0)=1$ . Among the many advantages of measuring the parity violating asymmetry is that  $F_{\text{wk}}$  is highly sensitive to the neutron distribution. This fact follows from the small weak charge of the proton that is strongly suppressed by the weak mixing angle:  $Q_{\text{wk}}^p = 1 - 4\sin^2\theta_W = 0.0719 \pm 0.0045$  [75]; instead, the weak charge of the neutron is large.

Given that the charge form factor is well known [60, 61], the parity violating asymmetry provides a model-independent determination of the weak form factor. One should note that Eq. (11) is valid in the plane-wave approximation. Indeed, both the parity conserving cross section given in Eq.(6) as well as the parity violating asymmetry are modified by Coulomb distortions. However, since Coulomb distortions are well understood [76, 77, 17, 78], we focus on the plane-wave versions as they provide a more intuitive picture of the underlying physics.

The Calcium Radius Experiment (CREX) [81] followed on the footsteps of the successful Lead Radius Experiment (PREX) [73, 74, 82]. Highlighting both experimental campaigns is the determination of the neutron skin thickness as an observable highly sensitive to the slope of the symmetry energy. Particularly interesting is the fact that the slope of the symmetry energy also correlates strongly to the radius of low mass neutron stars [83]. However, given that inferring the neutron skin thickness from the parity violating asymmetry involves some mild model dependence, it is preferable to focus on the model independent form factor.

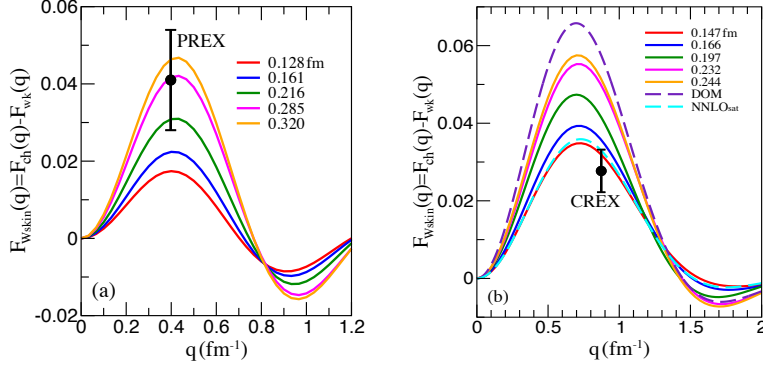


Figure 4: Theoretical predictions for the weak skin form factor of (a)  $^{208}\text{Pb}$  and (b)  $^{48}\text{Ca}$  are compared against the experimental values at the single value of the momentum transfer used for PREX ( $0.3977\text{ fm}^{-1}$ ) and CREX ( $0.8733\text{ fm}^{-1}$ ), respectively. Also shown are theoretical predictions using an ab initio approach with a chiral interaction (NNLOsat) [79] and a dispersive optical model (DOM) approach [80].

We show in Fig. 4 predictions for the weak skin form factor, defined as the difference between the charge and weak form factors:  $F_{\text{Wskin}}(q) \equiv F_{\text{ch}}(q) - F_{\text{wk}}(q)$ . Also shown are the experimental values for both  $^{208}\text{Pb}$  and  $^{48}\text{Ca}$  as quoted in Ref.[81]. Note that by expanding  $F_{\text{Wskin}}(q)$  at small momentum transfers one obtains

$$F_{\text{Wskin}}(q) \approx \frac{q^2}{6} (R_{\text{wk}}^2 - R_{\text{ch}}^2). \quad (12)$$

Thus, the curvature at the origin is proportional to the  $R_{\text{Wskin}} = R_{\text{wk}} - R_{\text{ch}}$ , a physical observable that is closely related to the neutron skin thickness  $R_{\text{skin}} = R_n - R_p$  [84].

The large value of  $F_{\text{Wskin}}^{208} = 0.041 \pm 0.013$  for  $^{208}\text{Pb}$  at the momentum transfer of the experiment ( $0.3977\text{ fm}^{-1}$ ) indicates that the weak form factor falls significantly faster than the corresponding charge form factor, a behavior often attributed to a large value for the neutron skin. Indeed, the PREX collaboration reported a neutron skin thickness of  $R_{\text{skin}}^{208} = 0.283 \pm 0.071\text{ fm}$  [82]. Based on these results—and taking advantage of the strong correlation between the neutron skin thickness of  $^{208}\text{Pb}$  and the slope of the symmetry energy [14, 15, 16, 17]—a large value of  $L = 106 \pm 37\text{ MeV}$  was deduced [45], which overestimates values extracted from both theoretical approaches and experimental measurements. From such a perspective, the three stiffest models, namely, the ones that predict the largest neutron skins in Fig. 4(a), are all consistent with the  $1\sigma$  PREX result.

Given that within the context of density functional theory a robust correlation emerges between the neutron skin thickness of medium to heavy neu-

tron rich nuclei and the corresponding neutron skin thickness of  $^{208}\text{Pb}$  (see Refs. [85, 86] and references contained therein) it came as a surprise to many to learn that CREX reported an unexpectedly small value for the weak skin form factor of  $^{48}\text{Ca}$  of  $F_{\text{Wskin}}^{48} = 0.0277 \pm 0.0055$  suggesting, in turn, a very thin neutron skin of  $R_{\text{skin}}^{48} = 0.121 \pm 0.035$  fm [81]. In this case—and in sharp contrast to the PREX analysis—only the softest of the five models is consistent with the CREX value. Besides the predictions from the five covariant EDFs, we also display in Fig. 4(b) theoretical predictions from an ab initio approach [79] and from a dispersive optical model (DOM) framework [80]. We note that the success of the ab initio prediction is noteworthy, especially as one of the main motivations behind CREX was the use of ab initio models to inform and improve the isovector sector of energy density functionals.

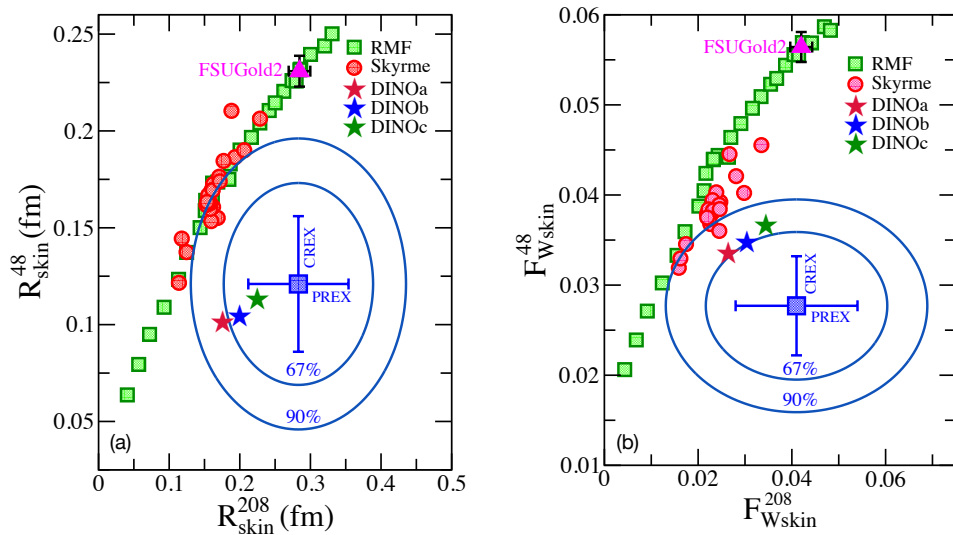


Figure 5: Predictions for the (a) the neutron skin thickness and (b) weak skin form factor of  $^{48}\text{Ca}$  and  $^{208}\text{Pb}$  for a large set of covariant (green squares) and a limited set of non-relativistic (pink) EDFs. The blue ellipses represent joint PREX and CREX 67% and 90% probability contours. The FSUGold2 prediction is included to illustrate typical statistical uncertainties. Finally, depicted with stars are the prediction of the three “DINO” models [87].

To further illustrate the tension in reconciling the PREX and CREX results, we display in Fig. 5 predictions for the neutron skin thickness and weak skin form factor of  $^{48}\text{Ca}$  and  $^{208}\text{Pb}$  for a large collection of covariant (RMF) and a limited set non relativistic (Skyrme) EDFs [87].

Also shown are experimental  $1\sigma$  error bars together with 67% and 90% probability contours. As it is clearly visible in the figure, none of these large number of EDFs can simultaneously describe the PREX and CREX results. Thus, in an effort to accommodate both results and motivated by a novel correlations

obeyed by the covariant EDFs, a new set of “DINO” functionals were calibrated using as input binding energies and charge radii of spherical nuclei as well as the PREX and CREX constraints. These results, depicted by the three stars, sit at or within of the 67% contour. However, this improvement comes at the expense of stiffening the equation of state which appears in contradiction with NICER constraints on the radius of a  $1.4 M_{\odot}$  neutron star [19, 20]. Ultimately, we must conclude that at present no single theoretical framework can account simultaneously for the properties of finite nuclei and neutron stars.

### 3.3 Coherent elastic neutrino nucleus scattering

Shortly after the discovery of weak neutral currents in 1973, coherent elastic neutrino-nucleus scattering (CEvNS) was proposed as a reaction with favorable cross sections that could impact a variety of astrophysical phenomena [88]. Since then, CEvNS has been recognized as a promising tool for the determination of neutron densities and supernovae detection [89, 90, 91, 92, 93, 94]. The differential cross for a neutrino scattering elastically from a spinless target in the laboratory frame is given by [90]

$$\left(\frac{d\sigma}{dT}\right) = \frac{G_F^2}{8\pi} M \left[2 - 2\frac{T}{E} - \frac{MT}{E^2}\right] Q_{\text{wk}}^2 F_{\text{wk}}^2(Q^2), \quad (13)$$

where  $E$  is the incident neutrino energy,  $M$  is the mass of the target nucleus,  $T$  the kinetic energy of the recoiling nucleus, and  $Q^2 = 2MT$ . The reaction is “favorable” because at forward angles the neutrino scatters coherently from the entire nucleus with a cross section that is proportional to the *square* of the weak charge of the nucleus  $Q_{\text{wk}}^2 = (NQ_{\text{wk}}^n + ZQ_{\text{wk}}^p)^2 \approx N^2$ . In analogy to Eq.(6), the CEvNS cross section is proportional to the square of the weak charge and probes the distribution of weak charge as a function of the momentum transfer. However, unlike elastic electron scattering, the scattered particle is undetectable. Hence, rather than detecting the outgoing neutrino one must measure the very low kinetic energy of the recoiling nucleus, a heroic feat that took four decades for its experimental realization [95]. As an illustration, the maximum kinetic energy of the recoiling nucleus is of the order of  $T_{\text{max}} \simeq 2E^2/M$ , which for neutrinos produced from pion decay at rest ( $E \simeq 30$  MeV) requires detection of nuclear recoils with only tens of keVs.

Besides its impact on a variety of astrophysical phenomena [88], CEvNS provides a portal to new physics. The nuclear weak charge  $Q_{\text{wk}}$  depends on the weak mixing angle, so a precise measurement of the cross section could potentially uncover new physics. However, the required precision is hindered by nuclear-structure effects contained in the weak form factor  $F_{\text{wk}}$ , which at low momentum transfers is dominated by the weak radius. Although CREX and PREX do not provide direct information on the weak radius of the noble gases being used as active targets for the detection of neutrinos as well as dark matter particles, one expects some correlation between the structure of neighboring nuclei, such as the weak form factor of  $^{48}\text{Ca}$  and the weak radius of  $^{40}\text{Ar}$ . A preliminary analysis conducted in the pre PREX-2-CREX era suggests a

strong correlation between the corresponding neutron skin thickness of  $^{48}\text{Ca}$  and  $^{40}\text{Ar}$  [96]. A more comprehensive analysis in the post PREX-2–CREX era is in progress. We note in closing that a good understanding of CEvNS is essential to assess the limitations of dark matter searches, as the so-called “neutrino floor”—recently renamed the “neutrino fog”—provides an irreducible background that imposes a severe penalty on dark-matter detection [97].

## 4 PREX/CREX experimental apparatus

There have been a number of measurements of nuclear weak form factors using PVES, including auxiliary measurements for the Qweak experiment, and dedicated measurements in the PREX/PREX-2 and CREX campaigns [98, 99, 100]. In this review we focus on the PREX-2 measurement, which has the strongest impact on the structure of neutron stars, although the experimental methods for CREX are similar. The experiments ran in Hall A of Jefferson Lab (JLab) located in Newport News, VA and use longitudinally polarized electrons that are incident on an isotopically pure solid target. Electrons scattered into the Hall A high resolution spectrometers are steered onto the detectors by a set of magnets. The detectors consist of thick and thin quartz detectors placed to capture the elastically scattered electrons while minimizing the contribution from inelastic processes. Although a more detailed explanation of the PREX and CREX experimental configurations may be found in Ref. [101], a brief summary will be provided here.

### 4.1 Parity-violating asymmetry in polarized electron scattering

Nuclear sizes have long been determined by measuring the charge form factor using parity-conserving elastic electron scattering. These experiments have painted the most accurate picture of the distribution of electric charge in atomic nuclei. In order to measure the corresponding weak-charge form factor which is largely determined by the neutron distribution, one must incorporate the contribution of the  $Z^0$  boson which couples preferentially to the neutrons in the target. This requires us to measure the parity-violating asymmetry, which results from the interference of two Feynman diagrams, one mediated by the photon and the other one by the  $Z^0$  boson. The “raw” or measured asymmetry,  $A_{\text{meas}}$  is the difference in the detector yields between scattering where the spin and momentum of the incident electron are parallel (right-handed) and anti-parallel (left-handed) over the sum. That is,

$$A_{\text{meas}} = \frac{Y_+ - Y_-}{Y_+ + Y_-} \quad (14)$$

Given that the asymmetry involves ratios of cross sections eliminates all corrections that come in as a multiplicative factor. Much of the experimental setup is designed to reduce and/or measure beam properties that can introduce a false

(non-parity-violating) asymmetry into the measured asymmetry. The whole accelerator—which consists of a racetrack with two linear accelerators and arcs at the ends and exits into the experimental halls—is depicted in Fig.6. As il-

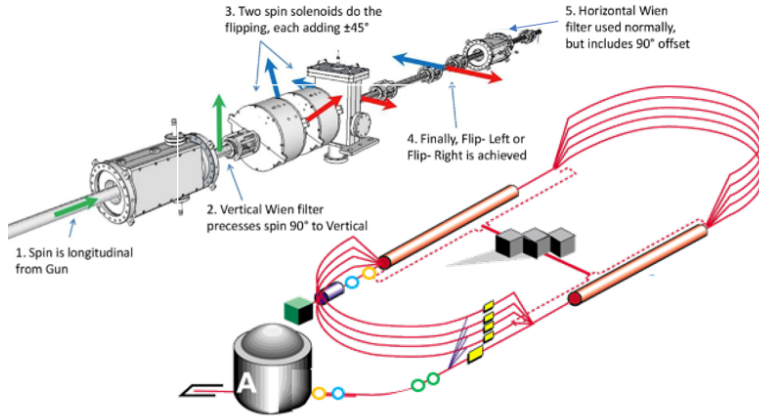


Figure 6: The lower right hand side of this figure provides a schematic view of the accelerator. The injector is represented by the green cube at the entrance to the north linac, the arcs then bend the electrons into the south linac for a total of six times to reach a maximum energy of 11 GeV in Hall A. The upper left hand side of the figure represents a schematic view of the spin manipulator which is located in the injector and allows us to change the direction of the spin of the beam to account for spin precession in the accelerator as well as to set examine the transverse polarization to quantify systematic uncertainties.

lustrated in the figure, one monitors the degree of polarization of the beam in the injector, which comes in as a dilution factor of the measured asymmetry, as well as beam properties such as charge, position, angle, and energy. In addition, one must correct for the asymmetries of background processes (which dilute the  $A_{PV}$ ) and for non-linearities in the detectors.

The longitudinally polarized electron beam is generated with a circularly polarized laser incident on a strained GaAs photocathode. The resulting electrons are longitudinally polarized, with either positive or negative helicity, depending on the direction of the circular polarization of the laser. The direction of the spin can be manipulated with a set of solenoids and Wien filters, and must be directed so that the electrons are fully longitudinal when they hit the target, after the spin precession that occurs in the magnets located in the accelerator arcs. The polarization of the laser can be flipped rapidly ( $\sim 2\text{kHz}$ ) so that asymmetries can be measured in randomly generated quartets (+ - -+ or - + +- , rather than pairs) on a timescale where the beam properties are consistent in the “helicity windows” of the quartet. The laser polarization is adjusted with the use of a Pockels cell, which ideally would not change the position or angle of the laser,

but in reality it does. This can introduce, in particular, charge asymmetries as the laser in the two polarization states is hitting parts of the photocathode with different quantum efficiencies. The charge asymmetry is measured with beam charge monitors throughout the accelerator and is minimized with a feedback system that can adjust the position of the laser on the photocathode. The beam positions, angles and energies are also monitored throughout the accelerator.

## 4.2 Special equipment for PREX

The PREX and CREX experiments used the Hall A High Resolution Spectrometers (HRSs). These consist of two spectrometer “arms”, left and right (L and

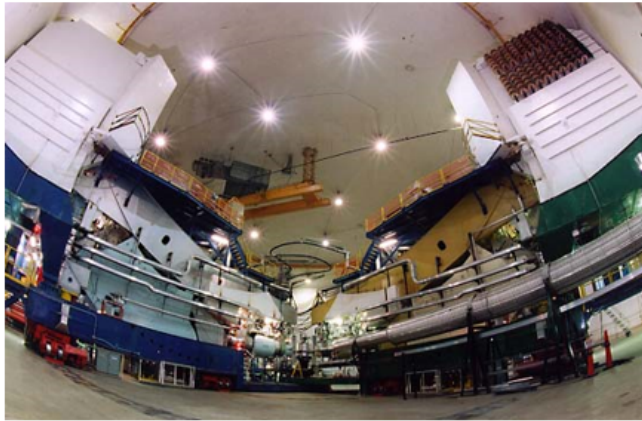


Figure 7: Picture of the two spectrometer arms in Hall A, from downstream beam right. The left HRS is on the right, behind the beamline (the grey tube) at a low angle (close to the beamline). The right HRS is on the left of this picture, at a very large angle relative to the beamline. The detector huts are the large, white boxes at the end of each of the HRSs.

R), with limited acceptance in both the horizontal plane (scattering angle) and out of plane (azimuthal angle). The spectrometers can rotate around the center of the hall, but their smallest angle relative to the downstream beamline is limited to  $\geq 12.5^\circ$ . Given that the figure-of-merit for PREX is optimized at  $\sim 5^\circ$ , the scattering chamber—which usually sits above the pivot of the HRSs—was moved upstream and a custom septum magnet was installed just upstream of the HRS to pre-bend the scattered electrons into the HRS. A precision collimator in the LHRS, with an exact mirror-image collimator in the RHRS, defines the angular acceptance of each of the arms and ensures that they are the same between the two spectrometer arms. Comparing the asymmetries measured in the LHRS and RHRS allow us to study and/or correct for a number of systematic uncertainties, including a parity-conserving asymmetry that depends on the azimuthal angle.

The lead ( $^{208}\text{Pb}$ ) target used in PREX was sandwiched between diamond plates and held in place mechanically in a copper frame. The diamond backing mitigates the melting of the target through heat transfer to the copper frame. The beam is also rastered on the target to spread the area with the heat load. For the PREX-2 run, the thickest diamond backing tested during PREX was chosen and a ladder with ten targets was prepared. In order to correct for the dilution from the diamond backing, special carbon runs were taken. The

Table 1: Corrections and systematic uncertainties to the measured PREX-2 parity-violating asymmetry of  $A_{PV}^{\text{meas}} = 550 \pm 16(\text{stat}) \pm 8(\text{sys})$  ppb [99].

Correction	Absolute [ppb]	Relative [%]
Beam asymmetry	$60.4 \pm 3.0$	$11.0 \pm 0.5$
Charge correction	$20.7 \pm 0.2$	$3.8 \pm 0.0$
Beam polarization	$56.8 \pm 5.2$	$10.3 \pm 1.0$
Target diamond foils	$0.7 \pm 1.4$	$0.1 \pm 0.3$
Spectrometer rescattering	$0.0 \pm 0.1$	$0.0 \pm 0.0$
Inelastic contributions	$0.0 \pm 0.1$	$0.0 \pm 0.0$
Transverse asymmetry	$0.0 \pm 0.3$	$0.0 \pm 0.1$
Detector nonlinearity	$0.0 \pm 2.7$	$0.0 \pm 0.5$
Angle determination	$0.0 \pm 3.5$	$0.0 \pm 0.6$
Acceptance function	$0.0 \pm 2.9$	$0.0 \pm 0.5$
Total correction	$17.7 \pm 8.2$	$3.2 \pm 1.5$

detectors consisted of a set of thick and thin quartz pieces, and a set of GEM trackers for studying the acceptance. Each HRS detector hut hosted a set of these detectors. The detector positions were set carefully in the detector plane to minimize the contribution from inelastic scattering, and the amount of rescattering in the spectrometer was studied in special runs. The amount of non-linearity was studied in bench tests.

We close this section by summarizing in Table 1 the size of the corrections made to the measured asymmetry and the uncertainties for each of the contributions to the systematic uncertainty. The resulting parity-violating asymmetry is  $A_{PV}^{\text{meas}} = 550 \pm 16(\text{stat}) \pm 8(\text{sys})$  ppb [99]. Unlike hadronic experiments that are plagued by model uncertainties, PREX is a statistically limited experiment.

## 5 Analysis of PREX/CREX data to extract the form factors

In this section we describe how to extract observables sensitive to the dynamics of neutron rich matter from the  $A_{PV}$  measurement described in the previous section. In particular, it is important to note that the determination of the weak



form factor extracted from  $A_{\text{PV}}$  is as model independent as the corresponding charge form factor extracted from parity-conserving experiments. In both cases Coulomb distortions must be taken into account, but these are well known [17, 76, 78]. Other quantities, such as the neutron skin, can then be related to the weak form factor, although these are slightly model dependent.

## 5.1 Calculation of form factors

To connect the parity-violating asymmetry to the neutron skin thickness one must start by computing various ground state properties. Given that both  $^{208}\text{Pb}$  and  $^{48}\text{Ca}$  are doubly-magic nuclei, their properties may be computed by solving the mean-field equations in the spherical limit [102]. Once the self-consistent solution is obtained, one can extract point proton and neutron densities. However, to compare against experiment one must take into account the finite size of the individual nucleons, as  $A_{\text{PV}}$  depends on both the charge and weak form factors. After incorporating single nucleon electromagnetic and weak form factors, the corresponding nuclear charge and weak form factors are given by the following expressions [74, 84]:

$$ZF_{\text{ch}}(q) = \sum_{i=p,n} \left( G_E^i(q) F_V^i(q) + \left( \frac{G_M^i(q) - G_E^i(q)}{1 + \tau} \right) \left[ \tau F_V^i(q) + \frac{q}{2m} F_T^i(q) \right] \right) \quad (15)$$

$$Q_{\text{wk}} F_{\text{wk}}(q) = \sum_{i=p,n} \left( \tilde{G}_E^i(q) F_V^i(q) + \left( \frac{\tilde{G}_M^i(q) - \tilde{G}_E^i(q)}{1 + \tau} \right) \left[ \tau F_V^i(q) + \frac{q}{2m} F_T^i(q) \right] \right) \quad (16)$$

where  $\tau = q^2/4m^2$ , the sum is over protons and neutrons,  $G_E$  and  $G_M$  are single-nucleon electric and magnetic Sachs form factors, respectively, and the tilde indicates the corresponding weak form factors. In turn,  $F_V$  and  $F_T$  are (point-nucleon) vector and tensor form factors. Nuclear charge and weak-charge densities may now be calculated from the corresponding form factors via a Fourier transform. That is,

$$\rho_{\text{ch}}(r) = \frac{Z}{2\pi^2 r} \int_0^\infty q \sin(qr) F_{\text{ch}}(q) dq, \quad (17)$$

$$\rho_{\text{wk}}(r) = \frac{Q_{\text{wk}}}{2\pi^2 r} \int_0^\infty q \sin(qr) F_{\text{wk}}(q) dq. \quad (18)$$

Note that the charge density  $\rho_{\text{ch}}(r)$  integrates to the total electric charge  $Z$ , whereas the weak-charge density  $\rho_{\text{wk}}(r)$  integrates to the total weak charge  $Q_{\text{wk}}$ .

The plane-wave expression for the parity-violating asymmetry given in Eq.(11) must be modified by including Coulomb distortions. Electrons scattering off a spherical nucleus satisfy the following Dirac equation:

$$\left( \boldsymbol{\alpha} \cdot \mathbf{p} + \beta m_e + \hat{V}(r) \right) \Psi = E \Psi, \quad (19)$$

where  $\alpha$  and  $\beta$  are Dirac matrices and the distorting potential  $\hat{V}(r)$  contains both vector and axial-vector components:

$$\hat{V}(r) = V(r) + \gamma^5 A(r). \quad (20)$$

Here  $V(r)$  is the standard Coulomb potential satisfying Poisson's equation with the nuclear charge density as its source and  $A(r)$  is the axial-vector potential given by

$$A(r) = \frac{G_F}{2^{3/2}} \rho_{\text{wk}}(r). \quad (21)$$

To ensure that the model behavior only enters in the weak sector, the nuclear charge density that generates the Coulomb potential is obtained from the experimental charge density, extracted from parity-conserving elastic electron scattering [103]. For (+/-) helicity states, the Dirac wavefunction becomes  $\Psi_{\pm} = \frac{1}{2}(1 \pm \gamma^5)\Psi$  and the potential becomes

$$\hat{V}(r) = V(r) \pm A(r). \quad (22)$$

In this manner, the positive helicity states scatter from the  $V_+ = V + A$  potential, whereas the negative helicity states scatter from the  $V_- = V - A$  potential. The difference in the cross sections relative to the sum, yields the parity violating asymmetry as in Eq.(11), but now with Coulomb distortions taken properly into account.

## 5.2 Connecting the model to the measured $A_{\text{PV}}$

Once the model calculations of have been completed, one must convolve the calculated parity-violating asymmetry  $A_{\text{PV}}^{\text{model}}$  with the acceptance of the spectrometers in order to compare against the experimental results. That is,

$$\langle A_{\text{PV}} \rangle = \frac{\int d\theta A_{\text{PV}}^{\text{model}}(\theta) \sin \theta \frac{d\sigma}{d\Omega} \epsilon(\theta)}{\int d\theta \sin \theta \frac{d\sigma}{d\Omega} \epsilon(\theta)}, \quad (23)$$

where  $d\sigma/d\Omega$  is the differential cross section and  $\epsilon(\theta)$  is the acceptance function, defined as the relative probability for an elastically scattered electron to arrive at the detector. Therefore, each model prediction of the weak-charge density  $\rho_{\text{wk}}(r)$  generates a unique value for  $A_{\text{PV}}$  which is then used to extract the nuclear observable and then compare against experiment.

The cleanest extracted observable from the measured  $A_{\text{PV}}$  is the weak form factor evaluated at the average  $q^2$  of the experiment. As alluded earlier and shown in Fig. 8 for CREX, this is because only the well-known Coulomb distortions affect the plane-wave expression given in Eq.(11). Given that the weak form factor is model independent, it is quoted without model error [82, 81]. Although not as strong, the correlation between  $A_{\text{PV}}$  and the weak radius may

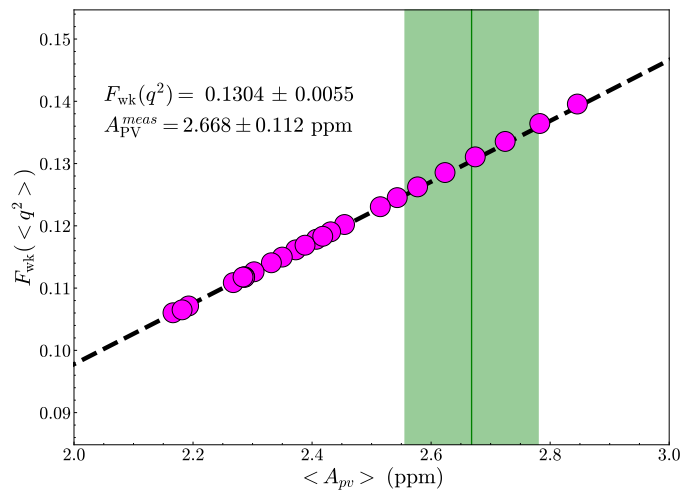


Figure 8: Weak form factor of  $^{48}\text{Ca}$  at the experimental  $q^2$  vs. model calculation of  $\langle A_{PV} \rangle$ . Here the magenta circles are the predictions of several density functionals, the black line is the least-squares fit to the functionals, and the green band represents the measured value of  $A_{PV}$  from CREX.

be calculated via the weak form factor, taking into account the point nucleon densities. By doing so, the neutron skin thickness of  $^{208}\text{Pb}$  was determined to be [99]

$$R_n - R_p = 0.278 \pm 0.078(\text{exp}) \pm 0.012(\text{theo}) \text{ fm}, \quad (24)$$

where now uncertainties in the surface thickness of  $^{208}\text{Pb}$  induce a small model (or theoretical) error.

## 6 Future measurements of neutron densities

In the future, both laboratory experiments and astrophysical observations will further our understanding of the dynamics of neutron rich matter. In this section we discuss the Mainz Radius Experiment (MREX) and expectations for continued and improved X-ray observations and gravitational wave detections.

### 6.1 The Mainz Radius EXperiment MREX

To perform experiments at the intensity and precision frontier, a new accelerator is currently under construction in Mainz. The layout of the Mainz Energy-recovering Superconducting Accelerator (MESA) [104] is shown in Fig.9 together with the some of the planned experiments, such as MAGIX, P2, and darkMESA.

The low energy ( $E_{\text{max}} = 155 \text{ MeV}$ ), high intensity ( $I = 150 \mu\text{A}$ ), and high-polarization ( $P \geq 85\%$ ) electron beam that MESA will provide offers ideal conditions for future high-precision PVES experiments to further constrain the EOS of neutron rich matter, primarily the slope of the symmetry energy  $L$ . The aim of MREX is to determine the neutron skin thickness of  $^{208}\text{Pb}$  to better than 0.03 fm, about a factor of two improvement over the precision of PREX-2; see Fig.5. As illustrated in Fig.9, MREX will use the P2 spectrometer/detector setup [105] to measure the elastically scattered electrons off  $^{208}\text{Pb}$ . The measurement will benefit from the full azimuthal coverage of the fused-silica Cherenkov detectors due to the solenoidal design of the spectrometer. This will allow for a significant reduction of the statistical uncertainty in the determination of the weak form factor and the extracted neutron skin thickness, which is currently the dominating contribution to the total uncertainty.

Preliminary rate estimates suggest that assuming a systematic uncertainty of 1% in the determination of the parity violating asymmetry, a  $\pm 0.03 \text{ fm}$  determination of the neutron skin thickness is feasible within 1500 hours of running time. Additional tracking simulations as well as more detailed simulations, including radiative corrections and background contributions, are ongoing. In an effort to further constrain the neutron density of  $^{208}\text{Pb}$ , we will determine for the first time its surface thickness by measuring the parity-violating asymmetry at the existing MAMI accelerator. Recall that for a heavy nucleus like  $^{208}\text{Pb}$ , a two-parameter symmetrized Fermi function accurately describes the entire density profile [106]; see Eq.(7). Given the current model uncertainty of 25%, the precision in both the PREX and MESA neutron skin determinations are limited by this uncertainty. Thus, an independent 10% measurement of the surface

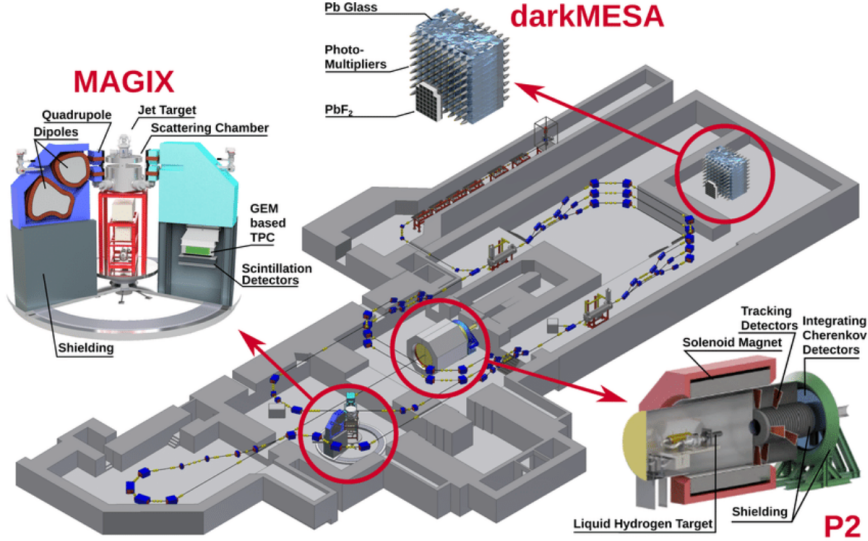


Figure 9: Layout of the new MESA facility with the experiments MAGIX, P2, and darkMESA [104]. MREX will use the P2 experimental setup shown in the bottom right corner of the figure. The liquid hydrogen target shown will be used for the measurement of the weak mixing angle [105] and will then be replaced by a  $^{208}\text{Pb}$  target to determine its weak form factor at the same momentum transfer as PREX-2.

thickness will reduce this contribution to a level below the error budget of the  $A_{\text{PV}}$  measurement [107]. The kinematics of the experiment is chosen to maximize the figure of merit, which in this case—in addition to the sensitivity of  $A_{\text{PV}}$  to the weak-charge radius—must be suppressed relative to the sensitivity to the surface thickness for the given beam energy and scattering angles. Preliminary rate estimates shows that this consideration is fulfilled for two configurations of the spectrometers and the beam energies of MAMI. Both possible scenarios are currently under investigation.

## 6.2 Future Astrophysical constraints to the equation of state

The mass-radius relation, which is in a one-to-one correspondence with the equation of state, is often regarded as the holy grail of neutron-star structure. We display in Fig.10 the mass-radius relation as predicted by the recently calibrated DINO models as well as other covariant density functionals that do not include a coupling to the  $\delta$ -meson [87]. The figure also displays simultaneous mass-radius determinations by the NICER mission for the two pulsars PSR J0030+045 [19, 20] and PSR J0740+6620 [21, 108]. With radii of about 15 km,

the predictions from all three DINO models are inconsistent at the 68% level with the NICER data for the low mass star [20]. Thus, we conclude that while the DINO models provide a plausible solution to the PREX-2–CREX dilemma, additional modifications to the isovector sector must be included in order to reduce its predictions for stellar radii.

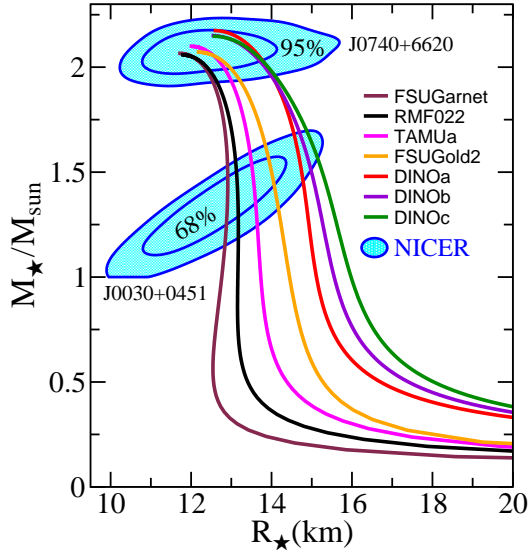


Figure 10: Mass-radius relation for neutron stars. Along with the three DINO models, predictions are also shown for a few covariant energy density functionals. The various ellipses display 68% and 95% confidence intervals extracted from NICER observations of the two pulsars PSR J0030+0451 [20] and PSR J0740+6620 [108].

Future X-ray observations of neutron stars will be performed with existing instruments such as NICER and by new missions. The high timing and energy resolution of NICER has greatly facilitated rationally resolved pulse profile measurements that infer the curvature of space. The European Space Agency Athena mission (scheduled to launch in the 2030s) will have a large aperture X-ray telescope and be able to observe fainter sources [109]. Future X-ray measurements may reduce statistical errors and will provide simultaneous mass-radius results for additional neutron stars. X-ray pulse profile measurements may still contain systematic errors due to the unavoidable modeling of the radiation from pulsar hot spots.

Gravitational-wave (GW) astronomy has opened a new window into the universe. What sets gravitational waves apart is their ability to unveil the inner workings of neutron stars in a unique manner complementary to electromagnetic waves. The next-generation GW observatories, such as the United States’ Cosmic Explorer and Europe’s Einstein Telescope, promise unparalleled sensi-

tivity. These new observatories will have the capability to detect binary neutron star mergers throughout the entire observable universe. Third-generation (3G) gravitational wave observatories will detect countless neutron star mergers, enabling the precise determination of stellar radii with a remarkable precision of 100 meters. Such unprecedented measurements of neutron star radii are poised not only to constrain the elusive nuclear equation of state but also to shed light on the composition of their interiors. The 3G era will pave the way for mapping the EOS of hot, dense, neutron-rich matter, offering profound new insights into the uncharted landscape of Quantum Chromodynamics.

## 7 CONCLUSION

Neutron stars and atomic nuclei offer fundamental insights into the dynamics of neutron rich matter. Although differing in size by 18 orders of magnitude, they are both made of the same constituents experiencing the same interactions. The historic detection of gravitational waves from the binary merger of neutron stars has opened a new window into the universe. Combined with more precise electromagnetic observations and laboratory experiments, such as PREX-2, CREX, and the future MREX, this new window will allow us to expand our understanding of neutron rich matter as never before. The dawn of the multi-messenger era has arrived and with it the golden era of neutron star physics. These are indeed exhilarating times for nuclear astrophysics.

## DISCLOSURE STATEMENT

The authors are not aware of any affiliations, memberships, funding, or financial holdings that might be perceived as affecting the objectivity of this review.

## ACKNOWLEDGMENTS

We would like to thank the PREX-2/CREX and P2 collaborations. We would also like to thank Anna Watts for providing data for mass-radius contours .

This material is based upon work which was supported by the German Research Foundation (DFG) via the individual grant Nr. 454637981) and the PRISMA<sup>+</sup> Cluster of Excellence, the U.S. Department of Energy Office of Science, Office of Nuclear Physics under Awards DE-FG02-87ER40365 (Indiana University) DE-FG02-92ER40750 (Florida State University), National Science Foundation grant PHY-2116686, Office of Nuclear Physics Contract No. DE-AC05-06OR23177, National Nuclear Security Administration of U.S. Department of Energy (Contract No. 89233218CNA000001), the Laboratory Directed Research and Development program of Los Alamos National Laboratory under project number XXW700, and National Science and Engineering Research Council (NSERC) grant number 322026 (University of Manitoba).

## References

- [1] J. M. Lattimer and M. Prakash, “The physics of neutron stars,” *Science*, vol. 304, no. 5670, pp. 536–542, 2004.
- [2] J. Lattimer, “Neutron stars and the nuclear matter equation of state,” *Annual Review of Nuclear and Particle Science*, vol. 71, no. 1, pp. 433–464, 2021.
- [3] A. Hewish, S. J. Bell, J. D. H. Pilkington, P. F. Scott, and R. A. Collins, “Observation of a rapidly pulsating radio source,” *Nature*, vol. 217, no. 5130, pp. 709–713, 1968.
- [4] A. Lam *et al.*, “Peeling apart a neutron star.” <https://astrobites.org/2014/08/11/peeling-apart-a-neutron-star/>, 2014. [Online; accessed September 1, 2023].
- [5] J. R. Oppenheimer and G. M. Volkoff, “On massive neutron cores,” *Phys. Rev.*, vol. 55, pp. 374–381, Feb 1939.
- [6] I. Vidana, A. Polls, A. Ramos, L. Engvik, and M. Hjorth-Jensen, “Hyperon effects on the properties of beta stable neutron star matter,” *Nucl. Phys. A*, vol. 691, pp. 443–446, 2001.
- [7] M. Oertel, F. Gulminelli, C. Providência, and A. R. Raduta, “Hyperons in neutron stars and supernova cores,” *Eur. Phys. J. A*, vol. 52, no. 3, p. 50, 2016.
- [8] M. Oertel, M. Hempel, T. Klähn, and S. Typel, “Equations of state for supernovae and compact stars,” *Rev. Mod. Phys.*, vol. 89, no. 1, p. 015007, 2017.
- [9] P. Demorest, T. Pennucci, S. Ransom, M. Roberts, and J. Hessels, “Shapiro delay measurement of a two solar mass neutron star,” *Nature*, vol. 467, p. 1081, 2010.
- [10] J. Antoniadis, P. C. Freire, N. Wex, T. M. Tauris, R. S. Lynch, *et al.*, “A Massive Pulsar in a Compact Relativistic Binary,” *Science*, vol. 340, p. 6131, 2013.
- [11] H. T. Cromartie *et al.*, “Relativistic Shapiro delay measurements of an extremely massive millisecond pulsar,” *Nat. Astron.*, vol. 4, no. 1, pp. 72–76, 2019.
- [12] E. Fonseca *et al.*, “Refined Mass and Geometric Measurements of the High-mass PSR J0740+6620,” *Astrophys. J. Lett.*, vol. 915, no. 1, p. L12, 2021.
- [13] M. G. Alford, A. Schmitt, K. Rajagopal, and T. Schafer, “Color superconductivity in dense quark matter,” *Rev. Mod. Phys.*, vol. 80, pp. 1455–1515, 2008.



- [14] B. A. Brown, “Neutron radii in nuclei and the neutron equation of state,” *Phys. Rev. Lett.*, vol. 85, p. 5296, 2000.
- [15] R. J. Furnstahl, “Neutron radii in mean-field models,” *Nucl. Phys.*, vol. A706, pp. 85–110, 2002.
- [16] M. Centelles, X. Roca-Maza, X. Viñas, and M. Warda, “Nuclear symmetry energy probed by neutron skin thickness of nuclei,” *Phys. Rev. Lett.*, vol. 102, p. 122502, 2009.
- [17] X. Roca-Maza, M. Centelles, X. Viñas, and M. Warda, “Neutron skin of  $^{208}\text{Pb}$ , nuclear symmetry energy, and the parity radius experiment,” *Phys. Rev. Lett.*, vol. 106, p. 252501, 2011.
- [18] J. Piekarewicz and M. Centelles, “Incompressibility of neutron-rich matter,” *Phys. Rev.*, vol. C79, p. 054311, 2009.
- [19] M. C. Miller *et al.*, “PSR J0030+0451 Mass and Radius from NICER Data and Implications for the Properties of Neutron Star Matter,” *Astrophys. J. Lett.*, vol. 887, p. L24, 2019.
- [20] T. E. Riley *et al.*, “A NICER View of PSR J0030+0451: Millisecond Pulsar Parameter Estimation,” *Astrophys. J. Lett.*, vol. 887, p. L21, 2019.
- [21] M. C. Miller *et al.*, “The Radius of PSR J0740+6620 from NICER and XMM-Newton Data,” *Astrophys. J. Lett.*, vol. 918, no. 2, p. L28, 2021.
- [22] B. P. Abbott *et al.*, “GW170817: Observation of Gravitational Waves from a Binary Neutron Star Inspiral,” *Phys. Rev. Lett.*, vol. 119, no. 16, p. 161101, 2017.
- [23] M. R. Drout *et al.*, “Light Curves of the Neutron Star Merger GW170817/SSS17a: Implications for R-Process Nucleosynthesis,” *Science*, vol. 358, pp. 1570–1574, 2017.
- [24] P. S. Cowperthwaite *et al.*, “The Electromagnetic Counterpart of the Binary Neutron Star Merger LIGO/Virgo GW170817. II. UV, Optical, and Near-infrared Light Curves and Comparison to Kilonova Models,” *Astrophys. J.*, vol. 848, no. 2, p. L17, 2017.
- [25] R. Chornock *et al.*, “The Electromagnetic Counterpart of the Binary Neutron Star Merger LIGO/VIRGO GW170817. IV. Detection of Near-infrared Signatures of r-process Nucleosynthesis with Gemini-South,” *Astrophys. J.*, vol. 848, no. 2, p. L19, 2017.
- [26] M. Nicholl *et al.*, “The Electromagnetic Counterpart of the Binary Neutron Star Merger LIGO/VIRGO GW170817. III. Optical and UV Spectra of a Blue Kilonova From Fast Polar Ejecta,” *Astrophys. J.*, vol. 848, no. 2, p. L18, 2017.

- [27] A. Bauswein, O. Just, H.-T. Janka, and N. Stergioulas, “Neutron-star radius constraints from GW170817 and future detections,” *Astrophys. J.*, vol. 850, no. 2, p. L34, 2017.
- [28] F. J. Fattoyev, J. Piekarewicz, and C. J. Horowitz, “Neutron skins and neutron stars in the multi-messenger era,” *Phys. Rev. Lett.*, vol. 120, no. 17, p. 172702, 2018.
- [29] E. Annala, T. Gorda, A. Kurkela, and A. Vuorinen, “Gravitational-wave constraints on the neutron-star-matter Equation of State,” *Phys. Rev. Lett.*, vol. 120, no. 17, p. 172703, 2018.
- [30] B. P. Abbott *et al.*, “GW170817: Measurements of neutron star radii and equation of state,” *Phys. Rev. Lett.*, vol. 121, no. 16, p. 161101, 2018.
- [31] E. R. Most, L. R. Weih, L. Rezzolla, and J. Schaffner-Bielich, “New constraints on radii and tidal deformabilities of neutron stars from GW170817,” *Phys. Rev. Lett.*, vol. 120, no. 26, p. 261103, 2018.
- [32] I. Tews, J. Margueron, and S. Reddy, “Critical examination of constraints on the equation of state of dense matter obtained from GW170817,” *Phys. Rev.*, vol. C98, no. 4, p. 045804, 2018.
- [33] T. Malik, N. Alam, M. Fortin, C. Providencia, B. K. Agrawal, T. K. Jha, B. Kumar, and S. K. Patra, “GW170817: constraining the nuclear matter equation of state from the neutron star tidal deformability,” *Phys. Rev.*, vol. C98, no. 3, p. 035804, 2018.
- [34] D. Radice, A. Perego, F. Zappa, and S. Bernuzzi, “GW170817: Joint Constraint on the Neutron Star Equation of State from Multimessenger Observations,” *Astrophys. J. Lett.*, vol. 852, no. 2, p. L29, 2018.
- [35] D. Radice and L. Dai, “Multimessenger Parameter Estimation of GW170817,” *Eur. Phys. J. A*, vol. 55, no. 4, p. 50, 2019.
- [36] I. Tews, J. Margueron, and S. Reddy, “Confronting gravitational-wave observations with modern nuclear physics constraints,” *Eur. Phys. J. A*, vol. 55, no. 6, p. 97, 2019.
- [37] C. D. Capano, I. Tews, S. M. Brown, B. Margalit, S. De, S. Kumar, D. A. Brown, B. Krishnan, and S. Reddy, “Stringent constraints on neutron-star radii from multimessenger observations and nuclear theory,” *Nature Astronomy*, vol. 4, pp. 625–632, 8 2019.
- [38] M. Tsang, W. Lynch, P. Danielewicz, and C. Tsang, “Symmetry energy constraints from GW170817 and laboratory experiments,” *Phys. Lett. B*, vol. 795, pp. 533–536, 2019.
- [39] C. Y. Tsang, M. B. Tsang, P. Danielewicz, W. G. Lynch, and F. J. Fattoyev, “Impact of the neutron-star deformability on equation of state parameters,” *Phys. Rev. C*, vol. 102, no. 4, p. 045808, 2020.

- [40] C. Drischler, R. Furnstahl, J. Melendez, and D. Phillips, “How Well Do We Know the Neutron-Matter Equation of State at the Densities Inside Neutron Stars? A Bayesian Approach with Correlated Uncertainties,” *Phys. Rev. Lett.*, vol. 125, no. 20, p. 202702, 2020.
- [41] P. Landry, R. Essick, and K. Chatziioannou, “Nonparametric constraints on neutron star matter with existing and upcoming gravitational wave and pulsar observations,” *Phys. Rev. D*, vol. 101, no. 12, p. 123007, 2020.
- [42] W.-J. Xie and B.-A. Li, “Bayesian inference of the dense-matter equation of state encapsulating a first-order hadron-quark phase transition from observables of canonical neutron stars,” *Phys. Rev. C*, vol. 103, no. 3, p. 035802, 2021.
- [43] R. Essick, I. Tews, P. Landry, and A. Schwenk, “Astrophysical Constraints on the Symmetry Energy and the Neutron Skin of Pb208 with Minimal Modeling Assumptions,” *Phys. Rev. Lett.*, vol. 127, no. 19, p. 192701, 2021.
- [44] K. Chatziioannou, “Uncertainty limits on neutron star radius measurements with gravitational waves,” *Phys. Rev. D*, vol. 105, no. 8, p. 084021, 2022.
- [45] B. T. Reed, F. J. Fattoyev, C. J. Horowitz, and J. Piekarewicz, “Implications of PREX-II on the equation of state of neutron-rich matter,” *Phys. Rev. Lett.*, vol. 126, no. 17, p. 172503, 2021.
- [46] F. Sammarruca and R. Millerson, “The Equation of State of Neutron-Rich Matter at Fourth Order of Chiral Effective Field Theory and the Radius of a Medium-Mass Neutron Star,” *Universe*, vol. 8, no. 2, p. 133, 2022.
- [47] T. Damour, M. Soffel, and C.-m. Xu, “General relativistic celestial mechanics. 2. Translational equations of motion,” *Phys. Rev.*, vol. D45, pp. 1017–1044, 1992.
- [48] E. E. Flanagan and T. Hinderer, “Constraining neutron star tidal Love numbers with gravitational wave detectors,” *Phys. Rev.*, vol. D77, p. 021502, 2008.
- [49] A. E. H. Love, “The yielding of the earth to disturbing forces,” *Proc. R. Soc. Lond.*, vol. A82, pp. 73–88, 1909.
- [50] T. Binnington and E. Poisson, “Relativistic theory of tidal Love numbers,” *Phys. Rev.*, vol. D80, p. 084018, 2009.
- [51] T. Damour, A. Nagar, and L. Villain, “Measurability of the tidal polarizability of neutron stars in late-inspiral gravitational-wave signals,” *Phys. Rev.*, vol. D85, p. 123007, 2012.

- [52] T. Hinderer, “Tidal Love numbers of neutron stars,” *Astrophys. J.*, vol. 677, pp. 1216–1220, 2008.
- [53] T. Hinderer, B. D. Lackey, R. N. Lang, and J. S. Read, “Tidal deformability of neutron stars with realistic equations of state and their gravitational wave signatures in binary inspiral,” *Phys. Rev.*, vol. D81, p. 123016, 2010.
- [54] T. Damour and A. Nagar, “Relativistic tidal properties of neutron stars,” *Phys. Rev.*, vol. D80, p. 084035, 2009.
- [55] S. Postnikov, M. Prakash, and J. M. Lattimer, “Tidal Love Numbers of Neutron and Self-Bound Quark Stars,” *Phys. Rev.*, vol. D82, p. 024016, 2010.
- [56] F. J. Fattoyev, J. Carvajal, W. G. Newton, and B.-A. Li, “Constraining the high-density behavior of the nuclear symmetry energy with the tidal polarizability of neutron stars,” *Phys. Rev.*, vol. C87, no. 1, p. 015806, 2013.
- [57] A. W. Steiner, S. Gandolfi, F. J. Fattoyev, and W. G. Newton, “Using Neutron Star Observations to Determine Crust Thicknesses, Moments of Inertia, and Tidal Deformabilities,” *Phys. Rev.*, vol. C91, no. 1, p. 015804, 2015.
- [58] J. Piekarewicz and F. J. Fattoyev, “Impact of the neutron star crust on the tidal polarizability,” *Phys. Rev. C*, vol. 99, no. 4, p. 045802, 2019.
- [59] R. Hofstadter, “Electron scattering and nuclear structure,” *Rev. Mod. Phys.*, vol. 28, pp. 214–254, 1956.
- [60] H. De Vries, C. W. De Jager, and C. De Vries, “Nuclear charge and magnetization density distribution parameters from elastic electron scattering,” *Atom. Data Nucl. Data Tabl.*, vol. 36, pp. 495–536, 1987.
- [61] G. Fricke, C. Bernhardt, K. Heilig, L. A. Schaller, L. Schellenberg, E. B. Shera, and C. W. de Jager, “Nuclear ground state charge radii from electromagnetic interactions,” *Atom. Data and Nucl. Data Tables*, vol. 60, p. 177, 1995.
- [62] I. Angeli and K. Marinova, “Table of experimental nuclear ground state charge radii: An update,” *At. Data Nucl. Data Tables*, vol. 99, pp. 69 – 95, 2013.
- [63] T. Suda *et al.*, “First Demonstration of Electron Scattering Using a Novel Target Developed for Short-Lived Nuclei,” *Phys. Rev. Lett.*, vol. 102, p. 102501, 2009.
- [64] T. Suda and H. Simon, “Prospects for electron scattering on unstable, exotic nuclei,” *Prog. Part. Nucl. Phys.*, vol. 96, pp. 1–31, 2017.

- [65] I. J. R. Aitchison and A. J. G. Hey, *Gauge Theories in Particle Physics, Second Edition*. Taylor & Francis, 1989.
- [66] J. D. Walecka, *Electron scattering for nuclear and nucleon structure*. New York: Cambridge University Press, 2001.
- [67] D. W. Sprung and J. Martorell, “The symmetrized Fermi function and its transforms,” *J. Phys. A*, vol. 30, pp. 6525–6534, 1997.
- [68] J. Piekarewicz, A. R. Linero, P. Giuliani, and E. Chicken, “Power of two: Assessing the impact of a second measurement of the weak-charge form factor of  $^{208}\text{Pb}$ ,” *Phys. Rev.*, vol. C94, no. 3, p. 034316, 2016.
- [69] R. D. Amado, J. P. Dedonder, and F. Lenz, “An Explicit Formula for Hadron - Nucleus Elastic Scattering in the Eikonal Approximation,” *Phys. Rev.*, vol. C21, pp. 647–661, 1980.
- [70] R. D. Amado, “Analytic insights into intermediate-energy hadron nucleus scattering,” *Adv. Nucl. Phys.*, vol. 15, pp. 1–42, 1985.
- [71] M. Thiel, C. Sfienti, J. Piekarewicz, C. J. Horowitz, and M. Vanderhaeghen, “Neutron skins of atomic nuclei: per aspera ad astra,” *J. Phys.*, vol. G46, no. 9, p. 093003, 2019.
- [72] T. Donnelly, J. Dubach, and I. Sick, “Isospin dependences in parity violating electron scattering,” *Nucl. Phys.*, vol. A503, p. 589, 1989.
- [73] S. Abrahamyan, Z. Ahmed, H. Albataineh, K. Aniol, D. S. Armstrong, *et al.*, “Measurement of the Neutron Radius of  $^{208}\text{Pb}$  Through Parity-Violation in Electron Scattering,” *Phys. Rev. Lett.*, vol. 108, p. 112502, 2012.
- [74] C. J. Horowitz, Z. Ahmed, C. M. Jen, A. Rakhman, P. A. Souder, *et al.*, “Weak charge form factor and radius of  $^{208}\text{Pb}$  through parity violation in electron scattering,” *Phys. Rev.*, vol. C85, p. 032501, 2012.
- [75] D. Androic *et al.*, “Precision measurement of the weak charge of the proton,” *Nature*, vol. 557, no. 7704, pp. 207–211, 2018.
- [76] C. J. Horowitz, “Parity violating elastic electron scattering and Coulomb distortions,” *Phys. Rev.*, vol. C57, pp. 3430–3436, 1998.
- [77] X. Roca-Maza, M. Centelles, F. Salvat, and X. Vinas, “Theoretical study of elastic electron scattering off stable and exotic nuclei,” *Phys. Rev.*, vol. C78, p. 044332, 2008.
- [78] O. Koshchii, J. Erler, M. Gorchtein, C. J. Horowitz, J. Piekarewicz, X. Roca-Maza, C.-Y. Seng, and H. Spiesberger, “Weak charge and weak radius of  $^{12}\text{C}$ ,” *Phys. Rev. C*, vol. 102, no. 2, p. 022501, 2020.

- [79] G. Hagen *et al.*, “Neutron and weak-charge distributions of the  $^{48}\text{Ca}$  nucleus,” *Nature Phys.*, vol. 12, no. 2, pp. 186–190, 2016.
- [80] M. H. Mahzoon, M. C. Atkinson, R. J. Charity, and W. H. Dickhoff, “Neutron Skin Thickness of  $^{48}\text{Ca}$  from a Nonlocal Dispersive Optical-Model Analysis,” *Phys. Rev. Lett.*, vol. 119, no. 22, p. 222503, 2017.
- [81] D. Adhikari *et al.*, “Precision Determination of the Neutral Weak Form Factor of  $\text{Ca48}$ ,” *Phys. Rev. Lett.*, vol. 129, no. 4, p. 042501, 2022.
- [82] D. Adhikari *et al.*, “Accurate Determination of the Neutron Skin Thickness of  $^{208}\text{Pb}$  through Parity-Violation in Electron Scattering,” *Phys. Rev. Lett.*, vol. 126, no. 17, p. 172502, 2021.
- [83] J. Carriere, C. J. Horowitz, and J. Piekarewicz, “Low mass neutron stars and the equation of state of dense matter,” *Astrophys. J.*, vol. 593, p. 463, 2003.
- [84] C. J. Horowitz and J. Piekarewicz, “Impact of spin-orbit currents on the electroweak skin of neutron-rich nuclei,” *Phys. Rev.*, vol. C86, p. 045503, 2012.
- [85] J. Piekarewicz, B. Agrawal, G. Colò, W. Nazarewicz, N. Paar, *et al.*, “Electric dipole polarizability and the neutron skin,” *Phys. Rev.*, vol. C85, p. 041302(R), 2012.
- [86] J. Piekarewicz, “Implications of PREX-2 on the electric dipole polarizability of neutron-rich nuclei,” *Phys. Rev. C*, vol. 104, no. 2, p. 024329, 2021.
- [87] B. T. Reed, F. J. Fattoyev, C. J. Horowitz, and J. Piekarewicz, “Density Dependence of the Symmetry Energy in the Post PREX-CREX Era,” *2305.19376*, 2023.
- [88] D. Z. Freedman, “Coherent Neutrino Nucleus Scattering as a Probe of the Weak Neutral Current,” *Phys. Rev.*, vol. D9, pp. 1389–1392, 1974.
- [89] C. J. Horowitz, K. J. Coakley, and D. N. McKinsey, “Supernova observation via neutrino - nucleus elastic scattering in the CLEAN detector,” *Phys. Rev.*, vol. D68, p. 023005, 2003.
- [90] K. Scholberg, “Prospects for measuring coherent neutrino-nucleus elastic scattering at a stopped-pion neutrino source,” *Phys. Rev.*, vol. D73, p. 033005, 2006.
- [91] K. Scholberg, “Supernova Neutrino Detection,” *Ann. Rev. Nucl. Part. Sci.*, vol. 62, pp. 81–103, 2012.
- [92] K. Patton, J. Engel, G. C. McLaughlin, and N. Schunck, “Neutrino-nucleus coherent scattering as a probe of neutron density distributions,” *Phys. Rev.*, vol. C86, p. 024612, 2012.

- [93] K. M. Patton, G. C. McLaughlin, and K. Scholberg, “Prospects for using coherent elastic neutrino-nucleus scattering to measure the nuclear neutron form factor,” *Int. J. Mod. Phys.*, vol. E22, p. 1330013, 2013.
- [94] M. Cadeddu, C. Giunti, Y. F. Li, and Y. Y. Zhang, “Average CsI neutron density distribution from COHERENT data,” *Phys. Rev. Lett.*, vol. 120, no. 7, p. 072501, 2018.
- [95] D. Akimov *et al.*, “Observation of Coherent Elastic Neutrino-Nucleus Scattering,” *Science*, vol. 357, no. 6356, pp. 1123–1126, 2017.
- [96] J. Yang, J. A. Hernandez, and J. Piekarewicz, “Electroweak probes of ground state densities,” *Phys. Rev. C*, vol. 100, no. 5, p. 054301, 2019.
- [97] D. Aristizabal Sierra, J. Liao, and D. Marfatia, “Impact of form factor uncertainties on interpretations of coherent elastic neutrino-nucleus scattering data,” *1902.07398*, 2019.
- [98] D. Androic *et al.*, “Determination of the  $^{27}\text{Al}$  Neutron Distribution Radius from a Parity-Violating Electron Scattering Measurement,” *Phys. Rev. Lett.*, vol. 128, no. 13, p. 132501, 2022.
- [99] D. Adhikari *et al.*, “Accurate Determination of the Neutron Skin Thickness of  $^{208}\text{Pb}$  through Parity-Violation in Electron Scattering,” *Phys. Rev. Lett.*, vol. 126, no. 17, p. 172502, 2021.
- [100] D. Adhikari *et al.*, “Precision Determination of the Neutral Weak Form Factor of Ca48,” *Phys. Rev. Lett.*, vol. 129, no. 4, p. 042501, 2022.
- [101] D. Adhikari *et al.*, “Precision Neutron Skins of  $^{208}\text{Pb}$  and  $^{48}\text{Ca}$  from Parity-Violating Electron Scattering,” *in preparation*, 2023.
- [102] C. J. Horowitz and B. D. Serot, “Self-consistent hartree description of finite nuclei in a relativistic quantum field theory,” *Nuclear Physics*, vol. A 368, pp. 503–528, Oct. 1981.
- [103] H. de Vries, C. W. de Jager, and C. de Vries, “Nuclear Charge-Density-Distribution Parameters from Electron Scattering,” *Atomic Data and Nuclear Data Tables*, vol. 36, p. 495, Jan. 1987.
- [104] N. B. et al., “The MESA Experimental Program: A Laboratory for Precision Physics with Electron Scattering at Low Energy,” *Nucl. Phys. News*, vol. 31, no. 3, p. 5, 2021.
- [105] D. B. et al., “The P2 experiment,” *Eur. Phys. J. A*, vol. 54, no. 11, p. 208, 2018.
- [106] C. J. Horowitz, J. Piekarewicz, and B. Reed, “Insights into nuclear saturation density from parity violating electron scattering,” *Phys. Rev. C*, vol. 102, no. 4, p. 044321, 2020.

- [107] B. Reed, Z. Jaffe, C. J. Horowitz, and C. Sfienti, “Measuring the surface thickness of the weak charge density of nuclei,” *Phys. Rev. C*, vol. 102, p. 064308, 2020.
- [108] T. E. Riley *et al.*, “A NICER View of the Massive Pulsar PSR J0740+6620 Informed by Radio Timing and XMM-Newton Spectroscopy,” *Astrophys. J. Lett.*, vol. 918, no. 2, p. L27, 2021.
- [109] K. Nandra and et al., “The hot and energetic universe: A white paper presenting the science theme motivating the athena+ mission,” *1306.2307*, 2013.